

Operation of silicon photomultipliers in a dilution refrigerator down to 9.4 mK towards a cryogenic cosmic ray muon veto system

QUEST-DMC Collaboration: A. Kemp,^a S. Autti,^b E. Bloomfield,^c A. Casey,^d N. Darvishi,^d N. Eng,^d P. Franchini,^c R. P. Haley,^b P. J. Heikkinen,^d A. Jennings,^e S. Koulosousas^{c,d} E. Leason,^{c,d} L. V. Levitin,^d J. March-Russell,^c A. Mayer,^b J. Monroe,^{a,c} D. Münstermann,^b M. T. Noble,^b J. R. Prance,^b X. Rojas,^d T. Salmon,^b J. Saunders,^d J. Smirnov,^f R. Smith,^a M. D. Thompson,^b A. Thomson,^b A. Ting,^d V. Tsepelin,^b S. M. West,^d L. Whitehead,^b D. E. Zmeev.^b

^aUKRI STFC Rutherford Appleton Laboratory, Particle Physics Department, Harwell, Didcot, OX11 0QX, UK.

^bDepartment of Physics, Lancaster University, Lancaster, LA1 4YB, UK.

^cDepartment of Physics, University of Oxford, Keble Road, Oxford, OX1 3RH, UK.

^dDepartment of Physics, Royal Holloway University of London, Egham, Surrey, TW20 0EX, UK.

^eRIKEN Center for Quantum Computing, RIKEN, Wako, 351-0198, Japan.

^fDepartment of Mathematical Sciences, University of Liverpool, Liverpool, L69 7ZL, UK.

E-mail: ashlea.kemp@stfc.ac.uk

ABSTRACT: We report the characterisation of a FBK NUV-HD-cryo silicon photomultiplier (SiPM) sensor operated in an 9.4 ± 0.2 mK environment inside a dilution refrigerator, towards the development of a cryogenic cosmic ray muon veto system to be operated internal to a dilution refrigerator required for low background experiments such as the QUEST-DMC dark matter search experiment. We characterise the single photon response and the gain (the charge produced per detected photon), the dark count noise rate, and correlated noise contributions as a function of operating voltage. This paper also reports first proof of concept measurements of using a SiPM directly coupled to scintillator in a 9.4 mK temperature environment, towards detecting candidate cosmic ray muon signals.

KEYWORDS: Cryogenic detectors; Photon detectors for UV, visible and IR photons (solid-state); Solid state detectors; Scintillators and scintillating fibres and light guides; Dark Matter detectors.

Contents

1	Introduction	1
2	Experimental setup	2
2.1	Hardware	2
2.2	I-V curve measurement and breakdown voltage	3
2.3	Data acquisition and processing	6
3	Characterisation analysis	7
3.1	Single photon response and gain	7
3.2	Dark count rate	9
3.3	Direct crosstalk	10
3.4	Correlated delayed avalanches	12
3.4.1	Enhanced afterpulsing at low temperatures	14
4	Towards a cryogenic cosmic ray muon veto system	16
5	Conclusions	18

1 Introduction

In recent years, silicon photomultipliers (SiPMs) have emerged as promising single photon detectors for use in particle physics, particularly in low background, rare-event search experiments such as direct dark matter detection experiments. Photomultiplier Tubes (PMTs) have long been the favoured technology for dark matter experiments, such as DEAP-3600 and LZ [1, 2], however compared to PMTs, SiPMs are cheaper to manufacture, require a lower operational voltage, and are insensitive to magnetic fields. In addition to their high gain and high photon detection efficiency, they can have a lower intrinsic radioactivity compared to PMTs. One drawback of SiPMs is that they generally exhibit higher intrinsic thermal noise than PMTs. However, since thermal noise decreases proportionally with temperature, it can be suppressed by operating the SiPMs at cryogenic temperatures.

Whilst limited, there have been measurements showing that SiPMs can operate close to liquid helium (LHe) temperatures and below [3–5], illustrating that there is a growing interest to demonstrate the viability of operating these sensors in sub-Kelvin conditions. As such, SiPMs are being explored by the QUEST-DMC collaboration as a potential photon sensor for use in a cryogenic cosmic ray muon veto system. The QUEST-DMC collaboration is developing, in one of its work packages, a direct dark matter search experiment projected to reach world-leading sensitivity to spin-dependent sub- GeV/c^2 mass dark matter using a superfluid helium-3 (^3He) target enclosed in a $\sim 1 \text{ cm}^3$ bolometer box [6–8]. The QUEST-DMC collaboration is operating bolometers at

Royal Holloway, University of London and Lancaster University, in ultra-low temperature dilution refrigerators fitted with an adiabatic demagnetisation stage capable of cooling ${}^3\text{He}$ to operating temperatures below 300 μK .

Since QUEST-DMC is currently operated at sea level, and not underground like the majority of dark matter experiments, cosmic ray induced background interactions will be a limiting factor for QUEST-DMC's dark matter search [9]. The cosmic ray muon veto system is currently in development; the baseline design makes use of a scintillator volume surrounding the bolometer cell at $\sim 300 \mu\text{K}$, where the exterior of this volume is coupled to the inner vacuum can which itself is coupled to the 10 mK stage of the dilution refrigerator, and is where the SiPM will be mounted. Therefore, 10 mK is the relevant temperature to characterise the SiPM in order to demonstrate the feasibility of this scheme. We are considering SiPMs over technologies traditionally deployed for photon detection in this temperature range due to the fact that they are large-area, commercially manufacturable, and simple to operate, compared with Superconducting Nanowire Single-Photon detectors (SNSPDs) which are much smaller, and Transition Edge Sensors (TESs) which have a relatively complex fabrication process.

SiPM technology has previously been used in cryogenic cosmic ray muon veto systems, such as the NUCLEUS experiment [10], which makes use of a plastic scintillator deployed in a dilution refrigerator at 850 mK. In this configuration, the plastic scintillator is instrumented with wavelength shifting fibres, and is coupled to a SiPM that is thermally coupled to the 300 K part of the cryostat. However, we are exploring the option of directly coupling SiPMs to the plastic scintillator itself, which would require the SiPM technology to be able to operate in $\sim \text{mK}$ environments. Without amplifier electronics and in the absence of light, a single NUV-HD-cryo SiPM with a surface area of $12 \times 8 \text{ mm}^2$ dissipates $\mathcal{O}(\text{pW})$ of power whilst it is biased, based on the device's properties measured at 77 K [11]. At this level of power dissipation, the heat load would be low enough such that a SiPM could be thermally coupled to a $\mathcal{O}(10\text{'s})$ mK temperature stage of a dilution refrigerator without disrupting the overall cooling power of the cryostat.

In this paper, we show the first operation of a NUV-HD-cryo SiPM [11] in a dilution refrigerator, demonstrating the feasibility of deploying this technology in a cryogenic cosmic ray muon system for the QUEST-DMC experiment. The SiPM is attached to the mixing chamber plate of the refrigerator, reaching a base temperature of $9.4 \pm 0.2 \text{ mK}$. Section 2 outlines the experimental setup, the data acquisition, and data processing chain. Section 3 describes the characterisation analysis that was performed. Section 4 reports first proof-of-principle measurements of using a SiPM directly coupled to a scintillator, and operated inside a dilution refrigerator.

2 Experimental setup

2.1 Hardware

We operate a single NUV-HD-cryo SiPM [11] of $12 \times 8 \text{ mm}^2$ inside a cryogen-free dilution refrigerator located at Royal Holloway, University of London. The dilution refrigerator is a modified Oxford Instruments Triton 200 [12]. A simplified schematic of the experimental setup is shown in Figure 1. The SiPM is mounted onto a custom PCB that distributes bias voltage and housed inside a 7 cm (L) x 3.8 cm (W) x 1.4 cm (D) copper box, which is attached to a copper stand that is thermally coupled to the plate of the mixing chamber.

The base temperature is measured using current sensing noise thermometry (CSNT) [13]. A CSNT sensor with resistance $2\text{ m}\Omega$ is mounted onto the ultra-low temperature plate, which is suspended from the mixing chamber plate using alumina tubes. The mixing chamber plate is thermally coupled to the ultra-low temperature plate via a flexible copper link. Whilst the data was acquired for this work, the base temperature as measured from the CSNT sensor on the ultra-low temperature plate, and thus, the mixing chamber plate, was $T_{\text{MC}} = 9.4 \pm 0.2\text{ mK}$. Further detail on the fridge design can be found in [14]. To ensure that the characterisation results we obtain actually reflect the SiPM operating in a 9.4 mK environment, we waited at least three days after cool-down to the mixing chamber base temperature before acquiring any data for this work. This allows for the plastic (FR-4) PCB on which the SiPM is mounted to thermalise to the same temperature as the copper.

As Figure 1 shows, all associated electronics are located outside of the dilution refrigerator at room temperature, including a custom-designed signal amplification board, providing a 130 V/V voltage gain. A Keysight E3649A provides the low-voltage supply required to power the board. A Keithley 2450 sourcemeter is used to deliver the bias voltage to the SiPM via the custom amplifier board and an external coaxial cable that connects to the top of the cryostat; an internal coaxial cable then delivers the bias voltage down to the SiPM mounted on the mixing chamber plate on the cold side. In addition, an LED that emits in the red wavelength range is attached to the outside of the copper box, where there is a 1 mm clearance hole allowing a direct line of sight from the LED to the SiPM. The LED is connected to a signal pulse generator via a current-limiting resistor, located outside of the dilution refrigerator, which is used to flash the LED for specific measurements, discussed in Section 2.2. Data is acquired with a Tetrox DPO72304DX 23 GHz bandwidth oscilloscope [15].

2.2 I-V curve measurement and breakdown voltage

We first measured the reverse I-V curve of the SiPM using the Keithley 2450 sourcemeter both at room temperature (prior to the cool-down), and after the cool-down to T_{MC} . The reverse I-V curve is used to characterise the relationship between the current flowing through the SiPM and the applied bias voltage, and to determine its breakdown voltage, defined as the minimum bias voltage above which the SiPM can operate in Geiger mode and detect single photons.

At cryogenic temperatures and in a dark environment, an external light source is required to observe the breakdown of the SiPM. A signal pulse generator (1 kHz , $999\text{ }\mu\text{s}$ pulse width) and a current-limiting resistor were used to bias the LED whilst the I-V curve was acquired. The reverse I-V was measured between $0 - 35\text{ V}$ in 300 mV steps; the current limit on the Keithley 2450 was set to $60\text{ }\mu\text{A}$ to avoid damage to the SiPM. Figure 3 (right) shows the measured reverse I-V curves of the SiPM acquired at T_{MC} (red) and at room temperature prior to the cool-down (green). We observed that whilst acquiring the I-V curve at T_{MC} , the temperature of the mixing chamber plate increased to $\sim 80\text{ mK}$ as a result of flashing the LED for approximately 15 seconds. After the reverse I-V curve was acquired and the LED was switched off, the temperature of the mixing chamber plate returned to T_{MC} within no more than 2 hours. We note that it is unlikely the temperature of the SiPM actually increased during the reverse I-V measurement, given the short duration (15 seconds) of heat injection and the low thermal conductivity of the SiPM PCB.

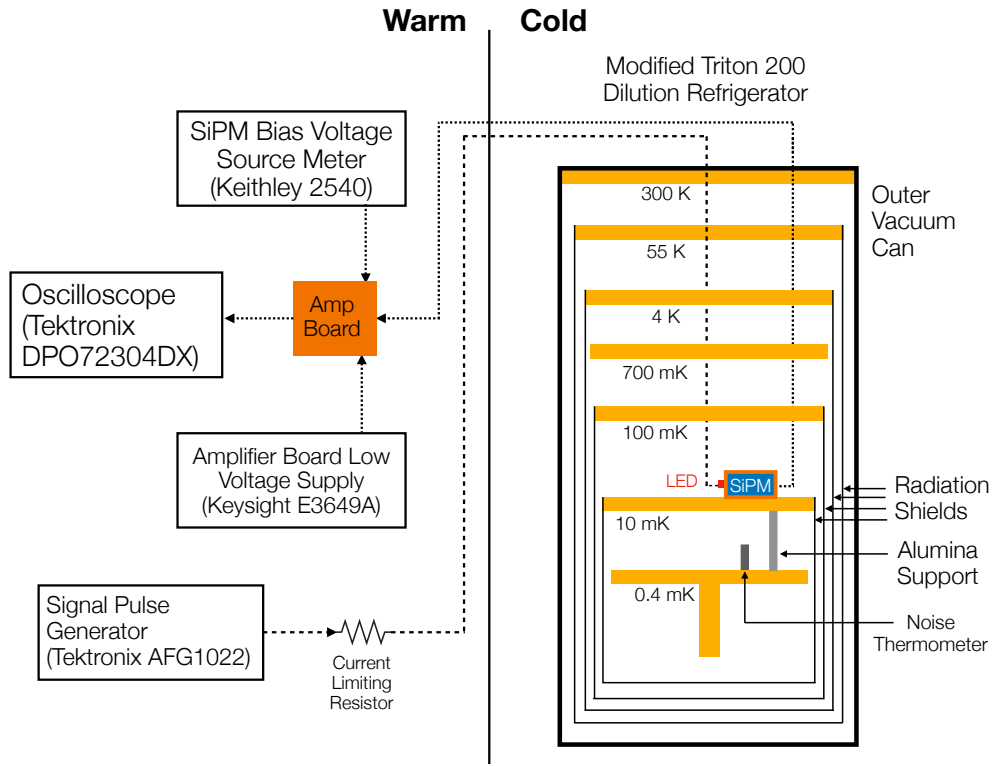


Figure 1. Simplified schematic diagram of the experimental setup used for the operation of a single NUV-HD-cryo SiPM in a cryogen-free dilution refrigerator.

The breakdown voltage, V_{bd} , can be calculated using the reverse I-V curve. The value of V_{bd} is temperature-dependent, and decreases as a function of lower temperatures [11]. However, it is expected that V_{bd} will eventually plateau and reach a minimum at a given temperature, such that there is no further reduction in V_{bd} for temperatures below this value. Our method to calculate V_{bd} is as follows. First, we calculate the derivative of the I-V curve, dI/dV , and then calculate the mean (μ) and standard deviation (σ) of dI/dV between $20 \text{ V} \leq V_{bias} \leq 25 \text{ V}$. V_{bd} is defined as the voltage at which dI/dV crosses a threshold of $\mu + 3\sigma$. Figure 3 (right) shows dI/dV as a function of V_{bias} , calculated from the I-V curve acquired at T_{MC} , with the threshold indicated by the horizontal red line.

The breakdown voltage of the SiPM at T_{MC} is calculated to be $V_{bd,MC} = 27.16 \pm 0.05 \text{ V}$, and at room temperature is $V_{bd,RT} = 32.18 \pm 0.07 \text{ V}$. These are indicated by the dashed red (green) lines on Figure 3 (left). As expected, the breakdown voltage decreases with lower temperatures. As the selected photon sensors for the upcoming DarkSide-20k dark matter experiment, the collaboration has tested 359040 NUV-HD-cryo SiPMs at 77 K, measuring several SiPM characteristics including the breakdown voltage. The DarkSide-20k collaboration determined the average breakdown voltage at 77 K to be $\bar{V}_{bd} = 27.19 \pm 0.05 \text{ V}$ [16]. This result is consistent with our measurement at T_{MC} , which indicates that there is no further reduction in V_{bd} for temperatures below 77 K for the NUV-HD-cryo technology.

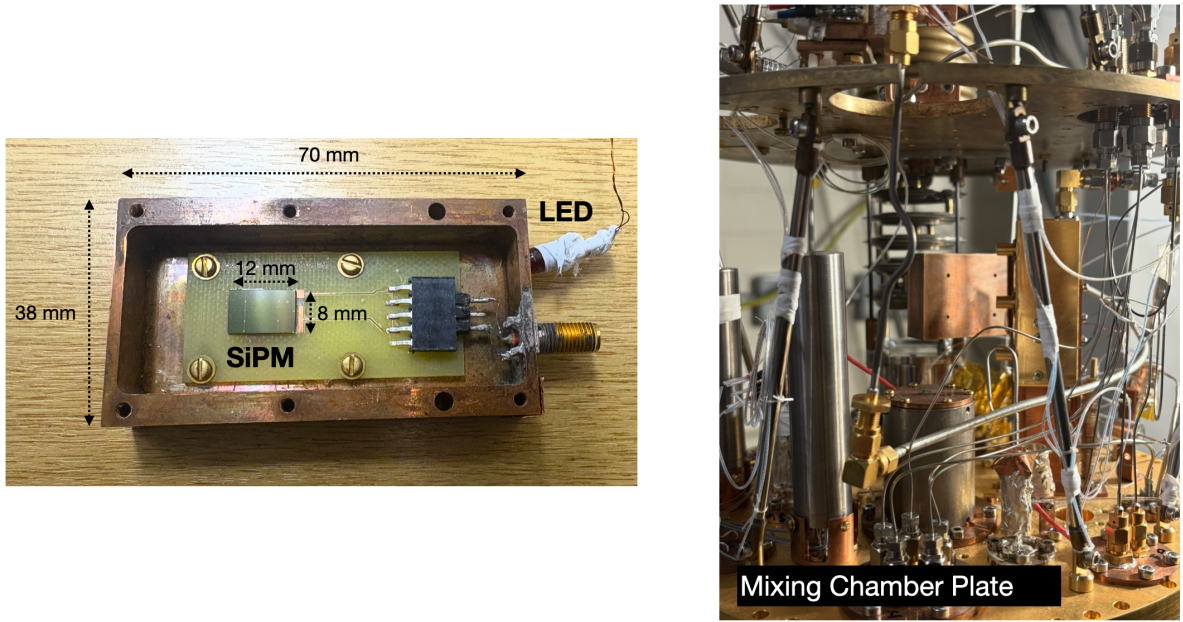


Figure 2. Left: Picture of the single NUV-HD-cryo SiPM tested in this work, mounted onto a PCB and housed inside a 7 cm (L) x 3.8 cm (W) x 1.4 cm copper box. An LED that emits in the red wavelength range is glued to the outside of the copper box, over a 1 mm clearance hole allowing direct line of sight to the SiPM for acquiring I-V curves in dark conditions. Right: Picture of the copper box (shown in left figure) mounted inside the dilution refrigerator. The copper box is attached to a copper stand thermally coupled to the mixing chamber plate, which reaches a base temperature of 9.4 ± 0.2 mK.

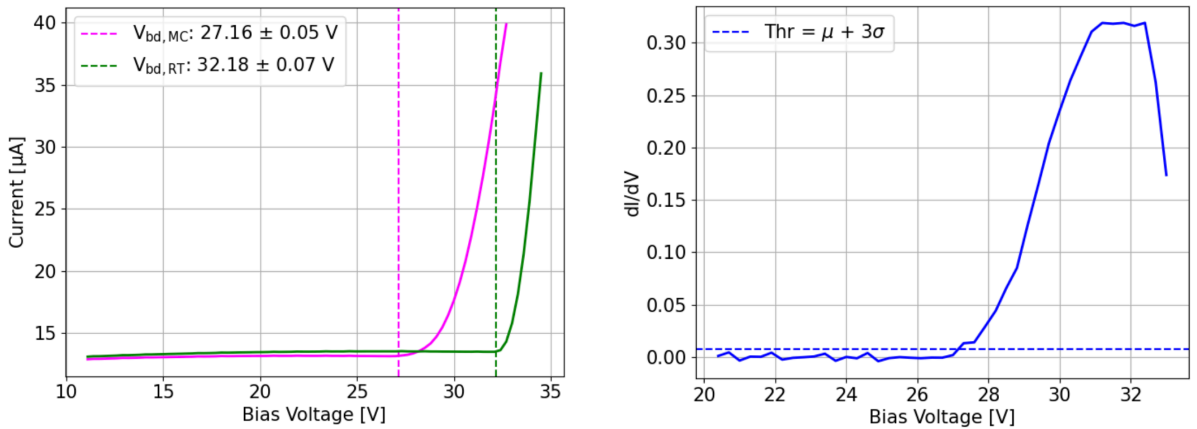


Figure 3. Left: Measured reverse I-V curve of the SiPM at T_{MC} (magenta) and room temperature (green), with breakdown voltages $V_{bd,MC} = 27.16 \pm 0.05$ V ($V_{bd,RT} = 32.18 \pm 0.07$ V) indicated by dashed red (green) lines. Right: Derivative of the reverse I-V curve, dI/dV , as a function of V_{bias} , acquired at T_{MC} . V_{bd} is defined as the voltage at which dI/dV crosses a threshold of $\mu + 3\sigma$, indicated by the blue dashed line.

We report all characterisation measurements in the following subsections as a function of both the operating bias voltage, V_{bias} , and the overvoltage, ΔV , defined as $\Delta V = V_{\text{bias}} - V_{\text{bd}}$.

2.3 Data acquisition and processing

We acquired three long datasets corresponding to three different operating bias voltages: $V_{\text{bias}} = 32, 33, 34$ V (equivalently $\Delta V = 4.8, 5.8, 6.8$ V). Each dataset was acquired in dark conditions, i.e., the LED was switched off. In principle, there should be no other external light reaching the SiPM, as this fridge is inherently dark due to the significant radiation shielding implemented to enable reaching ultra-low temperatures. Therefore, the only signals we expect to observe in these datasets should originate from thermally-induced intrinsic noise associated with the SiPM known as the dark count, plus any additional correlated noise sources. The dark count rate of the NUV-HD-cryo technology is expected to be extremely low, as it is measured to be <5 mHz/mm² at 77 K [11].

Approximately 30,000 waveforms were acquired in self-trigger mode per voltage. Data were acquired using the Tetroxix FastFrame Memory scheme [17], which segments the available memory in the oscilloscope such that each segment can be filled with a triggered acquisition at the desired sample rate with minimal dead time between the acquisitions. This is ideal for applications where pulses are separated by large intervals of inactivity in the signal [17], such as in our case. We acquire waveforms with a 250 MS/s sampling rate and a 100 μ s acquisition window, requiring a 5 μ s pre-trigger window. We set a 5 mV trigger level on the oscilloscope, which is terminated at 50 Ω , to trigger on the rising edge of the pulse. The trigger level was adjusted by eye in order to maximise triggers from real pulses and minimise triggers from electronics noise, and corresponds to approximately 90% of the mean height of a single photon pulse at $V_{\text{bias}} = 32$ V. Data is stored in a binary file format, saving the waveform data for each trigger, as well as the trigger time.

Each dataset is analysed using a simple pulse finding algorithm, in order to identify all candidate pulses in each 100 μ s-long waveform, and not just the pulse which triggered the event. This ensures that we accurately identify all single photon signals, some of which may have been missed during acquisition due to the 5 mV trigger level that was chosen to eliminate triggers from noise. In each 100 μ s-long waveform, a moving average filter is first applied to smooth out noise fluctuations. A baseline-subtracted waveform is computed using the baseline mean calculated in the first 3.2 μ s of the waveform, in the pre-trigger region. We then search for regions of the waveform which cross a given threshold for a certain consecutive number of samples, which can be identified as a candidate pulse. The threshold is set to 60% of the filtered mean height of a single photon pulse. We set a looser threshold in the pulse finding algorithm to ensure that we do not miss pulses with amplitudes <1 PE, which could occur from correlated delayed avalanches that occur within the SiPM recharge time. The time of the pulse, t_p , is defined as the time corresponding to the maximum amplitude of the waveform in the time-over-threshold region. A “prompt” pulse charge is calculated by integrating the waveform between $[t_p - 100 \text{ ns} : t_p + 250 \text{ ns}]$. Sections 3.3 and 3.4 discuss in more detail why we choose to calculate a prompt pulse charge, rather than a full pulse charge.

Figure 4 shows an example waveform acquired at $V_{\text{bias}} = 32$ V ($\Delta V = 4.8$ V), corresponding to a single dark count rate signal, which is equivalent to the single photon signal. The raw waveform (blue), the baseline-subtracted and filtered waveform (orange), the pulse finding threshold (red), and the identified pulse time (green) are shown. In addition to the pulse time, pulse amplitude,

and pulse charge, we determine the absolute time difference between the current pulse and the preceding pulse, dt , calculated using the time of the pulses within their respective waveforms, the unix timestamp of the waveforms, and the fraction of a second past the unix timestamps of the waveforms. All of this information is then stored in a data file upon which the downstream characterisation analysis described in Section 3 is performed.

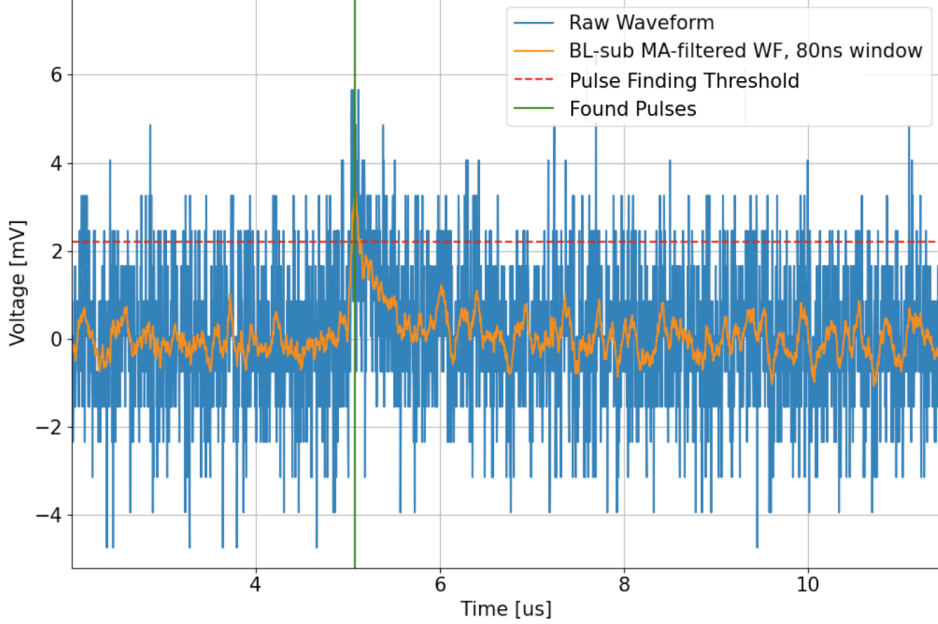


Figure 4. Example waveform acquired at $V_{\text{bias}} = 32$ V ($\Delta V = 4.8$ V), corresponding to a single dark count rate signal (equivalent to the single photon signal). Raw waveform (blue), baseline-subtracted and filtered waveform (orange), pulse finding threshold (red), and identified pulse time (green) are shown.

3 Characterisation analysis

In this section, we describe the characterisation measurements performed on waveform data acquired from the NUV-HD-cryo SiPM whilst operated at T_{MC} .

3.1 Single photon response and gain

We first characterise the single photoelectron (PE) response of the SiPM. To do this, we plot two histograms corresponding to the prompt pulse charge and pulse amplitude respectively of all found pulses in a given run. Figure 5 shows the amplitude (left) and prompt charge (right) distributions of the SiPM whilst operated at $V_{\text{bias}} = 32$ V ($\Delta V = 4.8$ V). In both histograms, there are distinct peaks for successive numbers of PE. The first peak is the 1 PE signal, and corresponds to the integrated charge or amplitude of the observed output current pulse following the detection of a single photon. The pedestal peak is not visible in our distributions since a requirement is made on the pulse height in the pulse finding algorithm applied to the data, to limit identifying false pulses originating from electronic noise.

Due to intrinsic noise, a SiPM still generates output pulses in the absence of light. The 1 PE peak we observe in our distributions is due to a combination of thermally-induced noise called “dark counts” and noise from “correlated delayed avalanches”. These noise sources are discussed in detail in Sections 3.2 and 3.4 respectively. The successive peaks corresponding to >1 PE we observe in our distributions are a result of correlated noise from “direct crosstalk”, which manifest as superpositions of the 1 PE waveform. This noise source is discussed further in Section 3.3.

The single PE response is determined by fitting a gaussian to the first peak in each spectrum and extracting the fitted mean. The amplitude and prompt charge of the single PE peak at $V_{\text{bias}} = 32$ V ($\Delta V = 4.8$ V) is calculated to be $\bar{A}_{1\text{PE}} = 3.65 \pm 0.42$ mV and $\bar{Q}_{1\text{PE}} = 0.15 \pm 0.02$ Vs respectively. The single PE amplitude is smaller than the trigger level used during acquisition (5 mV) due to the moving average filter which is applied to the data prior to running the pulse finding algorithm, which reduces the height of the pulses; this can be seen in Figure 4.

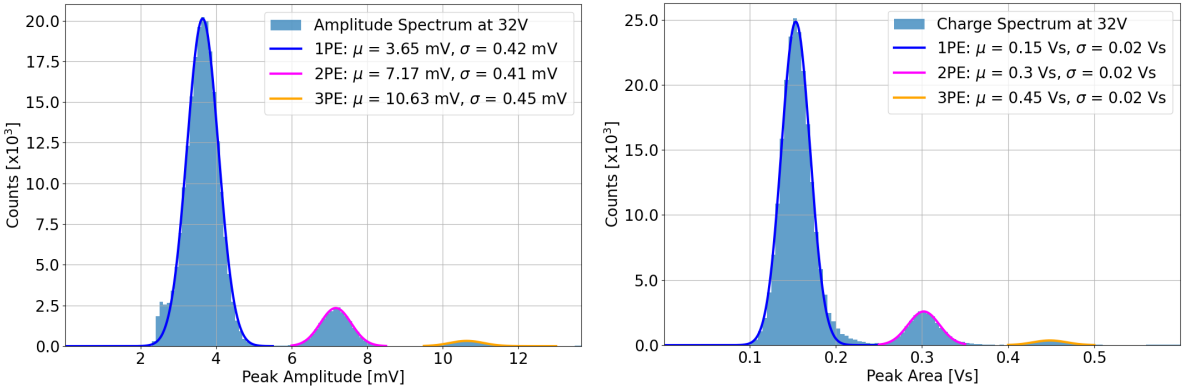


Figure 5. Pulse amplitude (left) and pulse prompt charge (right) distributions of the NUV-HD-cryo SiPM operated at $V_{\text{bias}} = 32$ V ($\Delta V = 4.8$ V). Gaussian functions are fit to the first 3 peaks in each histogram in order to extract the gain measured in amplitude (left) and charge (right). The first peak in each histogram corresponds to the 1 PE peak.

With the single PE response, we can now calculate the gain, defined as the amount of charge generated in an avalanche in response to each detected photon. Each microcell in the SiPM produces a highly quantised amount of charge when a photon is absorbed in the active volume, and this response is extremely uniform across all microcells. This unique property of SiPMs results in excellent charge resolution, and allows for a very precise measurement of the gain. The gain is expected to be proportional with ΔV [18].

The separation between each pair of consecutive peaks in Figure 5 is constant and constitutes the gain. To determine the separation, we fit individual gaussian functions to the remaining peaks in each spectrum. We compute the gain as the difference in the fitted means for the first and second peaks, $G = \mu_{2\text{PE}} - \mu_{1\text{PE}}$. The gain measured from the amplitude and charge distributions at $V_{\text{bias}} = 32$ V ($\Delta V = 4.8$ V) are $G_A = 3.52 \pm 0.006$ mV and $G_Q = 0.149 \pm 0.0003$ Vs respectively.

Figure 6 shows the measured gain as a function of V_{bias} (ΔV) calculated using charge (blue) and amplitude (red) respectively. The gain calculated from the charge, G_Q , can be converted to the gain in units of the number of charge carriers produced in an avalanche, G_{N_e} , using the following

equation:

$$G_{N_e} = \frac{G_Q \cdot t_S}{R_{\text{scope}} \cdot G_{\text{amp}} \cdot q_e}, \quad (3.1)$$

where $R_{\text{scope}} = 50 \Omega$ is the input resistance of the oscilloscope, and $G_{\text{amp}} = 130 \text{ V/V}$ is the gain of the custom amplifier board from the design specification. The multiplication factor of t_S , the time difference between adjacent waveform samples, accounts for the oscilloscope sampling rate. As expected, we observe a proportional increase in the gain with ΔV . The measured gain ranges between 6×10^5 and 9×10^5 for $4.8 \text{ V} < \Delta V < 6.8 \text{ V}$, which is consistent with typical SiPM gain values of 10^5 – 10^7 [18].

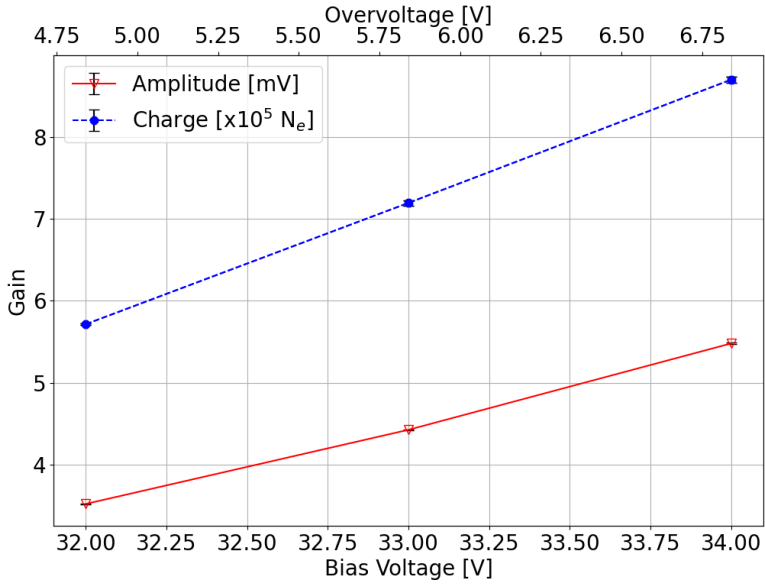


Figure 6. Gain of NUV-HD-cryo SiPM in charge in $[10^5 N_e]$ (blue), and amplitude in [mV] (red) as a function of V_{bias} (ΔV). Solid red and dashed blue lines are interpolated between the data points. Error bars are shown, however are not necessarily visible as the errors are small.

3.2 Dark count rate

SiPMs can exhibit both uncorrelated and correlated noise contributions. The dark count rate (DCR) is the main source of uncorrelated noise. Each dark count is initiated by a thermally-generated charge carrier, which triggers an avalanche in the active region through the same process as a photon-generated charge carrier; thus DCR events are indistinguishable from single photon signals. The DCR of the SiPM is expected to increase with ΔV [11], since a higher ΔV increases the probability of an avalanche being triggered. The DCR is also expected to increase as a function of temperature. At higher temperatures, the DCR is dominated by field-enhanced thermal generation of charge carriers. However, below a certain temperature, the reduction of the DCR reaches a plateau, where the DCR becomes dominated by tunnelling effects that are weakly temperature dependent.

We characterise the DCR of the NUV-HD-cryo SiPM using the unshadowing method, based on using the time distribution between two consecutive pulses described in [19]. Given the incredibly low DCR of this technology, we also consider the time differences of pulses across separate waveforms, assuming that a negligible number of pulses are lost between waveforms. This assumption can be made due to the data being acquired using the Tetrox FastFrame Memory scheme [17] described earlier in Section 2.3, which has a maximum dead time of 2.5 μ s.

To select primary pulses for this analysis, we first apply the pulse finding algorithm to the data to identify all candidate ≥ 1 PE pulses. We also require that the time difference between the primary pulse and the previous pulse is ≥ 50 μ s. This cut is made to reduce the probability of the secondary pulse not being associated with the selected primary pulse to be negligible. Figure 7 (left) shows the measured time distribution of consecutive pulses whilst the SiPM is operated at $V_{\text{bias}} = 32$ V ($\Delta V = 4.8$ V). The dip in the dt distribution at close to the waveform acquisition window, 100 μ s, can be primarily attributed to a loss in the pulse finder efficiency for pulses that are spread across two continuous waveforms.

Figure 7 (right) shows the unshadowed time distribution following the procedure in [19]. The unshadowed distribution is the average number of secondary pulses occurring between the bin limits of t_i and t_{i+1} defined in Figure 7 (left), normalised per unit time to determine the pulse rate. The pulse rate distribution contains two contributions: the correlated delayed pulse rate, and the DCR. At large times, the rate of correlated delayed pulses is expected to disappear, leaving only the DCR. To extract the DCR, we compute the weighted mean of the asymptotic rate, between 1 s $< dt <$ 8 s. We calculate the DCR to be 3.89 ± 0.19 mHz/mm² at $V_{\text{bias}} = 32$ V ($\Delta V = 4.8$ V), the value of which is indicated by the horizontal dashed line in Figure 7 to guide the eye.

Figure 8 shows the measured DCR as a function of V_{bias} (ΔV). As expected, the DCR increases as a function of ΔV , increasing by 25% for 4.8 V $< \Delta V < 6.8$ V. These values are also consistent with the measured DCR value of <5 mHz/mm² at 77 K from [11] and are compatible with the observation that for temperatures below 77 K, the DCR is dominated by tunnelling effects which are weakly temperature-dependent and thus in this regime, the DCR is approximately constant for falling temperature.

3.3 Direct crosstalk

Optical crosstalk is a source of correlated noise in a SiPM that occurs due to the emission of a small number of photons ($\sim 10^{-5}$ photons/electron) during an avalanche [20], which can trigger avalanches in the surrounding microcells. Optical crosstalk can be split into two categories:

1. Direct crosstalk (DiCT) occurs when a photon directly generates charge carriers in the active region of a neighbouring microcell, resulting in an almost simultaneous avalanche with respect to the primary avalanche.
2. Delayed crosstalk (DeCT) occurs when a photon generates charge carriers outside of the active region of a neighbouring microcell. The charge carriers can diffuse to the active region of the microcell, triggering a delayed avalanche.

DiCT manifests as a superposition with the 1 PE (single photon) pulse. For example, if a primary avalanche triggers two secondary crosstalk avalanches, the resulting output pulse will

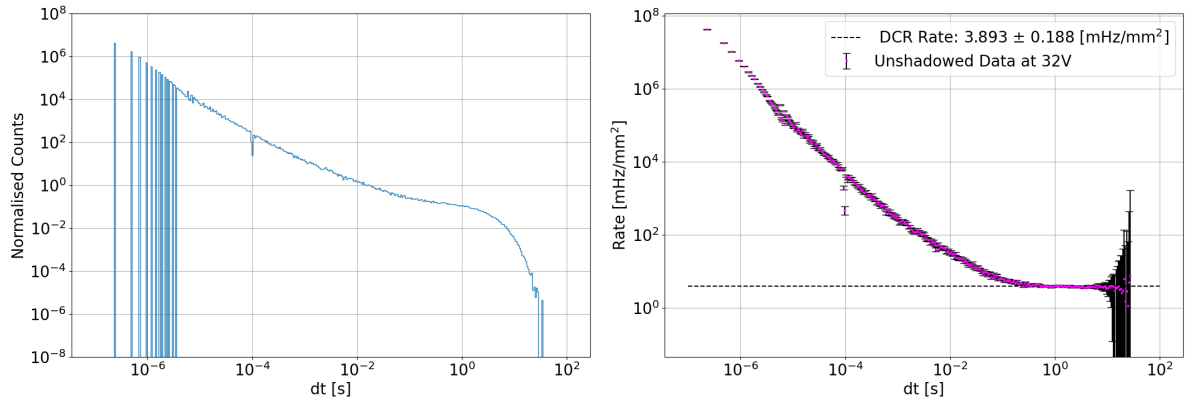


Figure 7. Left: Measured time distribution (dt) of consecutive pulses at $V_{\text{bias}} = 32$ V ($\Delta V = 4.8$ V). Right: Unshadowed time distribution, based on dt distribution in left-hand plot. Horizontal dashed line indicates calculated DCR of 3.893 ± 0.19 mHz/mm 2 .

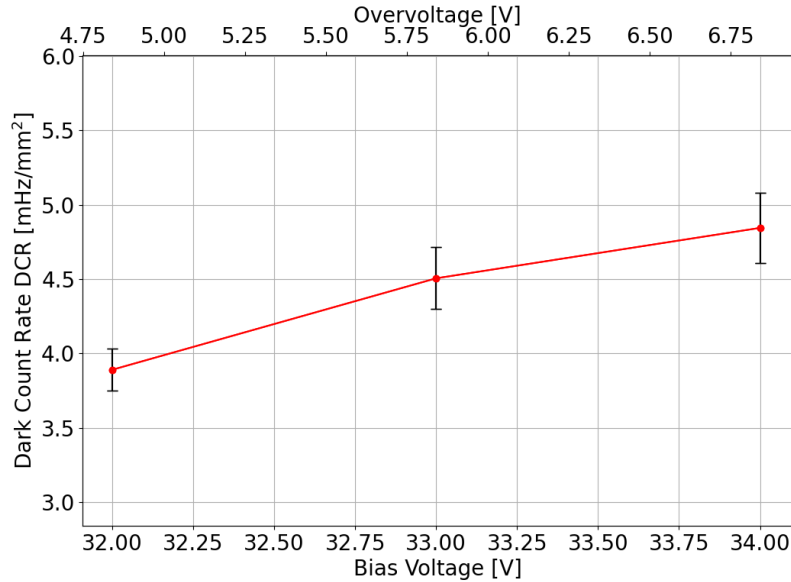


Figure 8. Measured DCR of NUV-HD-cryo SiPM as a function of V_{bias} (ΔV). The DCR increases by 25% between $4.8 \text{ V} < \Delta V < 6.8 \text{ V}$. Red line is interpolated between the data points.

be a 3 PE pulse. DiCT can therefore be a limiting factor for applications requiring accurate photon-counting, since it artificially increases the number of detected photons and degrades the signal-to-noise ratio. The DiCT probability is expected to increase with ΔV , since the probability of an avalanche increases with ΔV . In addition, the number of emitted photons is linearly proportional to ΔV , which also contributes to an increase in the DiCT probability. There appears to be a weak dependence on the DiCT probability with temperature for the NUV-HD-cryo SiPM technology, as reported in [11].

To characterise the DiCT of the SiPM, we calculate the mean number of additional prompt avalanches per primary, (\bar{N}_{APA}), defined as:

$$\bar{N}_{\text{APA}} = \frac{1}{N} \sum_{i=1}^N \frac{Q_i}{\bar{Q}_{\text{1PE}}} - 1, \quad (3.2)$$

where Q_i is the charge of each identified pulse, \bar{Q}_{1PE} is the average 1 PE charge, and N is the number of pulses analysed. In practise, we compute \bar{N}_{APA} by normalising the amplitude distribution shown in Figure 5 by the average 1 PE amplitude, \bar{A}_{1PE} , to align the peaks on the x -axis with the number of PE they correspond to. We then take the mean of the normalised histogram and subtract 1 to determine \bar{N}_{APA} , shown in Figure 9 for an operating voltage of $V_{\text{bias}} = 32$ V ($\Delta V = 4.8$ V).

We choose the amplitude distribution instead of the charge distribution for this analysis due to the fact that for increasing ΔV , we start to observe an additional “shoulder” feature forming in the tails of the peaks in the charge distribution. This is an artifact of the charge integration window used in this analysis: if correlated delayed avalanches (CDAs) following an avalanche occur within the charge integration window of the pulse of interest, $[t_p - 100 \text{ ns} : t_p + 250 \text{ ns}]$, part or all of the CDA pulse(s) will be included in the charge integral of the pulse of interest, skewing the charge distribution. Figure 9 (right) shows the pulse charge distribution of the NUV-HD-cryo SiPM operated at the higher bias voltage of $V_{\text{bias}} = 34$ V ($\Delta V = 6.8$ V), clearly showing a shoulder forming in the tail of the 1 PE peak. This artifact is suppressed in the amplitude distribution, since each filled entry in the distribution corresponds to the amplitude from each, individual identified pulse, regardless of whether it originates from DCR or CDAs.

An additional cut is made on the normalised amplitude distribution before determining the mean in order to remove any identified pulses with amplitudes < 1 PE, attributed either to electronic noise or to CDAs that occur on short timescales after the primary avalanche (i.e., before the SiPM has had a chance to recover following a discharge). Using the fitted mean (μ_{1PE}) and standard deviation (σ_{1PE}) from the gaussian fit to the 1 PE peak, we remove any pulses from the distribution with amplitudes $< \mu_{\text{1PE}} - 3\sigma_{\text{1PE}}$. Figure 9 (left) shows the normalised amplitude distribution at an operating voltage of $V_{\text{bias}} = 32$ V ($\Delta V = 4.8$ V). The purple vertical line indicates the mean of the distribution, corresponding to $\bar{N}_{\text{APA}} = 0.170 \pm 0.002$. Figure 10 shows \bar{N}_{APA} as a function of ΔV . As expected, \bar{N}_{APA} increases as a function of ΔV , increasing by 64% across $4.8 \text{ V} < \Delta V < 6.8 \text{ V}$.

At 77 K, the DiCT probability is reported to be 13% at $\Delta V = 5$ V for the NUV-HD-cryo technology [11], whilst our measurement of $\bar{N}_{\text{APA}} = 0.170 \pm 0.002$ at $\Delta V = 4.8$ V corresponds to a DiCT probability of $16\% \pm 0.2\%$ ¹. Whilst this could suggest a small increase in the DiCT probability when operating at T_{MC} , this difference could also be attributed to small differences between data selection and analysis choices, i.e., our decision to cut on pulse amplitudes of $< \mu_{\text{1PE}} - 3\sigma_{\text{1PE}}$.

3.4 Correlated delayed avalanches

CDAs are a type of correlated noise in SiPMs, comprised of DeCT and afterpulses (AP). DeCT events occur within very short timescales, typically $\mathcal{O}(10 \text{ ns})$ after the primary avalanche, whereas AP events tend to occur on longer timescales, $\mathcal{O}(\text{ns} - \mu\text{s})$.

¹The DiCT probability is calculated using the mean number of additional prompt avalanches with the following equation: $P = 1 - e^{-\bar{N}_{\text{APA}}}$.

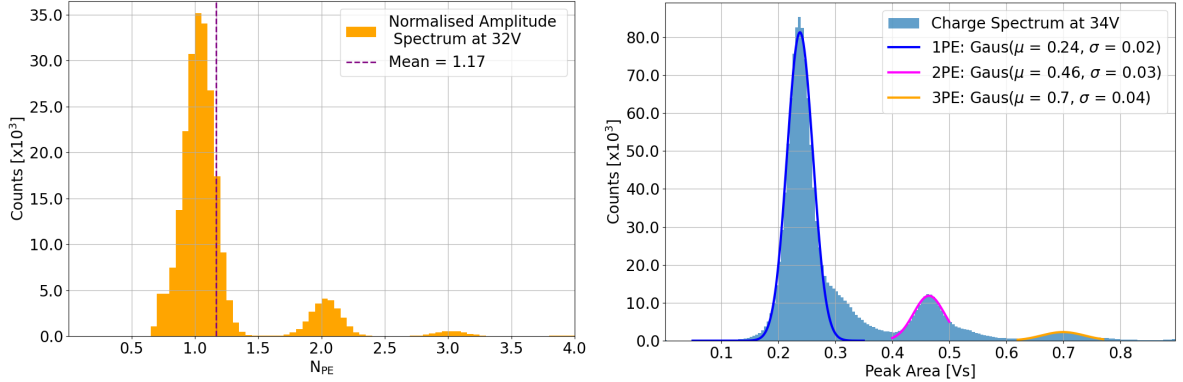


Figure 9. Left: Normalised amplitude distribution at $V_{\text{bias}} = 32$ V ($\Delta V = 4.8$ V), used to determine \bar{N}_{APA} . The purple vertical line indicates the mean of the distribution, corresponding to $\bar{N}_{\text{APA}} = 0.170 \pm 0.002$. Right: Pulse charge distribution at $V_{\text{bias}} = 34$ V ($\Delta V = 6.8$ V), illustrating a clear shoulder forming in the tail in the 1 PE peak due to enhanced CDA probability at higher ΔV .

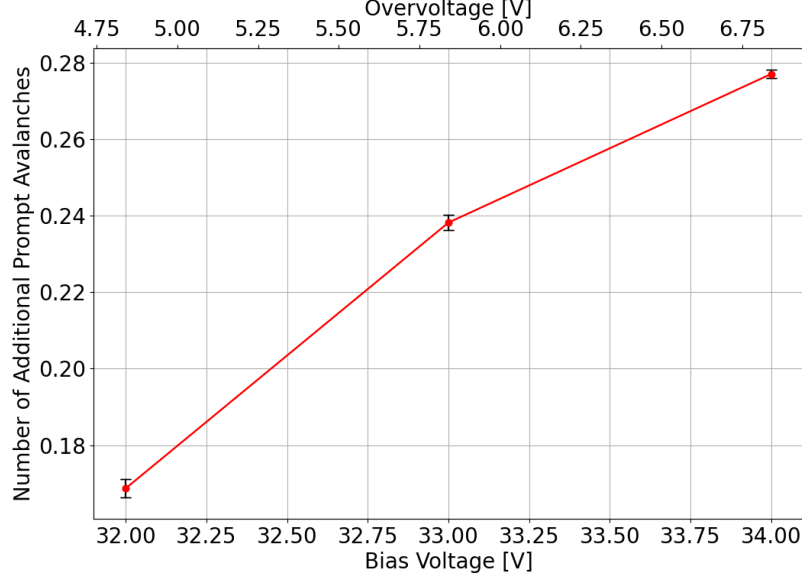


Figure 10. Mean number of additional prompt avalanches, \bar{N}_{APA} , as a function of ΔV . \bar{N}_{APA} increases by 64% for $4.8 \text{ V} < \Delta V < 6.8 \text{ V}$. Solid red line is interpolated between the data points.

Afterpulsing is a process in which charge carriers generated in an avalanche can become trapped within defects of the silicon structure. Trapped charge carriers are then subsequently released, which can trigger avalanches in the same microcell after the primary avalanche has occurred. A single primary avalanche can result in multiple APs as a result of numerous trapped charge carriers being released at different timescales, or due to an AP triggering a second AP. If the timescale of the AP is short compared to the characteristic recharge time of the SiPM, the gain of the AP-induced avalanche is smaller than the primary avalanche, resulting in a pulse amplitude less than the 1 PE amplitude. If the timescale of the AP is long compared to the characteristic recharge time of the SiPM, APs are indistinguishable from 1 PE signals induced either thermally (from DCR) or optically (from a photon).

Similarly to DiCT, APs artificially increase the number of detected photons. APs can also distort integration measurements for high photon fluxes, effectively serving as an additional gain factor for the measured signal. The AP probability is expected to increase with ΔV [11], since a higher ΔV results in a larger initial avalanche charge. This, combined with an increase in the probability of an avalanche, results in a higher AP probability.

We determine the mean number of CDAs, \bar{N}_{CDA} , within three different time windows following a primary avalanche: 1 μs , 5 μs , and 10 μs . The mean number of CDAs is calculated on a waveform-by-waveform basis. For each waveform, we count how many subsequent pulses are found within a 1 μs , 5 μs , and 10 μs window after the primary pulse (i.e., the first pulse in the waveform that caused the trigger to occur). We apply no requirement on the amplitude of pulses found $<1 \mu\text{s}$ with respect to the primary pulse, since the gain is decreased for APs occurring within the SiPM recharge time. However, for pulses detected $\geq 1 \mu\text{s}$ from the primary pulse, we apply a requirement on the pulse amplitude to be $\geq \mu_{\text{1PE}} - 3\sigma_{\text{1PE}}$, to reduce leakage from electronic noise. We make one additional requirement, that the time difference between the primary pulse of a waveform p_i and the last pulse of the preceding waveform p_{i-1} is $\geq 1 \text{ s}$. This cut is made to ensure that the primary pulse originates from DCR or from a photon-induced PE, and is not a CDA of a previous pulse. The choice of 1 s is informed from the unshadowed time distribution in Figure 7, which shows the asymptotic rate from pure DCR at time differences $\geq 1 \text{ s}$.

Figure 11 shows the mean number of CDAs as a function of ΔV , within a 1 μs (red), 5 μs (blue), and 10 μs (green) window following a primary avalanche. The mean number of CDAs is measured to be $\bar{N}_{\text{CDA}} = 0.170 \pm 0.002$ (1 μs window), 0.420 ± 0.003 (5 μs window), and 0.560 ± 0.004 (10 μs window) at $\Delta V = 4.8 \text{ V}$. \bar{N}_{CDA} increases by 102% (1 μs window), 146% (5 μs window), and 172% (10 μs window) between $\Delta V = 4.8 \text{ V}$ and $\Delta V = 6.8 \text{ V}$. The mean number of CDAs increases as a function of ΔV as expected, driven by the increase in AP probability for higher ΔV . We also observe an increase in the mean number of CDAs for longer time windows following a primary avalanche for a given ΔV value.

3.4.1 Enhanced afterpulsing at low temperatures

At 77 K, the AP probability is reported to be 12% at $\Delta V = 5 \text{ V}$ [11]. We determine an AP probability of 43% at $\Delta V = 4.8 \text{ V}$ ² assuming a 10 μs integration window, as is typically considered

²The AP probability is calculated using the mean number of correlated delayed avalanches with the following equation: $P = 1 - e^{-\bar{N}_{\text{CDA}}}$.

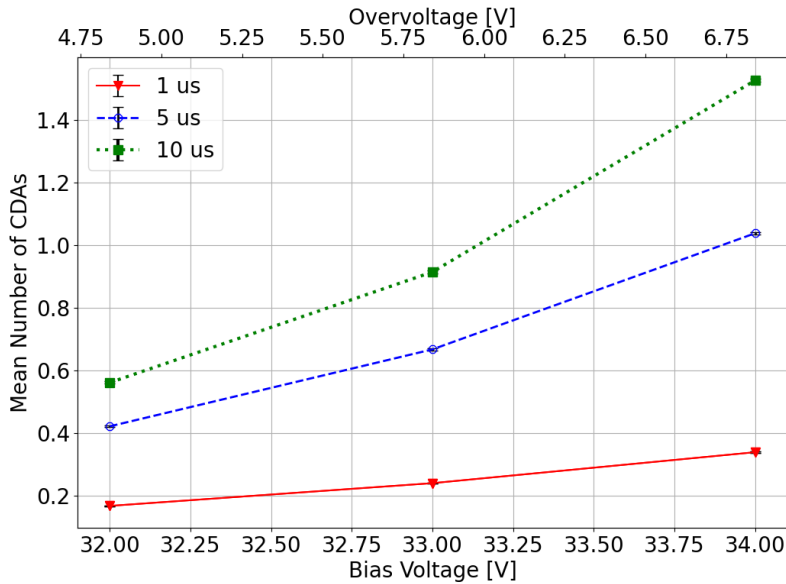


Figure 11. Mean number of CDAs, \bar{N}_{CDA} , within a 1 μs (red), 5 μs (blue), and 10 μs (green) window following a primary avalanche as a function of ΔV . \bar{N}_{CDA} increases by 102% (1 μs window), 146% (5 μs window), and 172% (10 μs window) between $\Delta V = 4.8$ V and $\Delta V = 6.8$ V. Solid red, dashed blue, and dotted green lines are interpolated between the data points. Error bars are shown, however are not necessarily visible as the errors are small.

for computing AP probabilities in SiPMs [21, 22]. We also assume that the number of DeCT events contributing to the mean number of CDAs we measure is negligible, and that the CDAs we observe originate predominately from AP. We make this assumption based on the timescale of DeCT events, which occur at delay times < 20 ns, which we do not have the ability to resolve from the primary avalanche in our data.

We observe a substantial increase in the AP probability at T_{MC} compared to the measured value at 77 K. This behaviour has previously been reported at temperatures below 40 K [4, 5]. It has also been observed that below 40 K, the average time difference between a primary avalanche and AP(s) increases. We also see evidence for an increase in the delay times of APs with respect to the primary avalanche. The dt distribution shown in Figure 7 shows long tails that extend significantly beyond the typical AP timescale of 10 μs . This is indicative of delayed APs that continue to occur even at long timescales, $\mathcal{O}(\text{ms})$.

The combination of a higher AP probability and an increase in the average time delay of APs can result in long-lasting AP “trains”, in which APs trigger further APs, causing a self-sustaining cascade of APs that can last for a long time at ultra-low temperatures, up to approximately 1 ms [4]. This effect is driven by the temperature-dependent trapping and release of charge carriers, discussed in [23]. Figure 12 shows an example waveform trace acquired at $V_{\text{bias}} = 34$ V ($\Delta V = 6.8$ V), consistent with a self-sustaining AP train. The presence of such AP trains clearly limits the photon-counting ability of the SiPM, particularly at higher ΔV values. Whilst delayed APs will also distort integration measurements over $\mathcal{O}(\text{ms})$ timescales, Figure 11 shows that the level of distortion

caused by delayed APs can be mitigated by using shorter integration windows and operating at a lower ΔV .

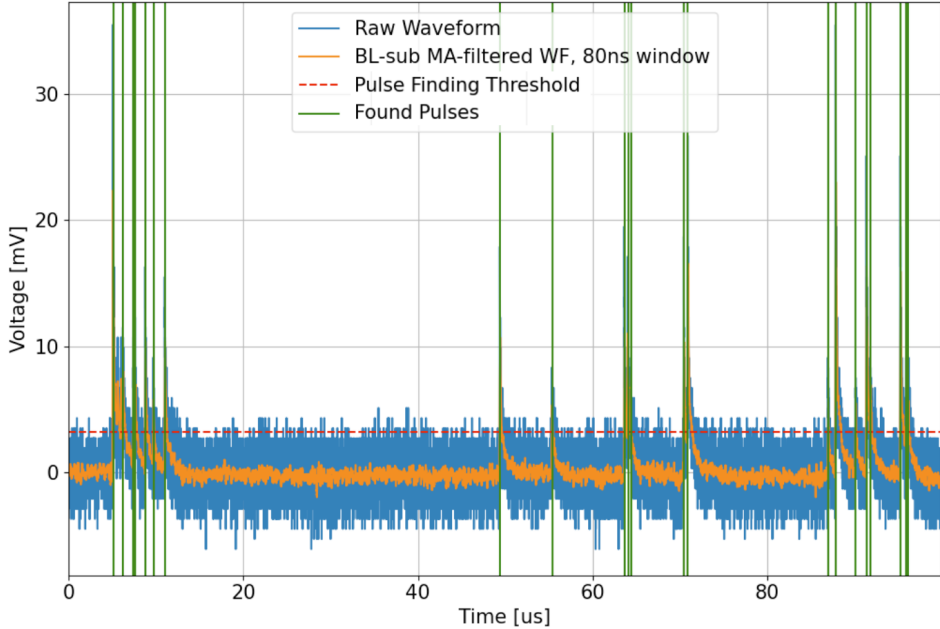


Figure 12. Example waveform trace acquired at $V_{\text{bias}} = 34$ V ($\Delta V = 6.8$ V), illustrating long-lasting APs consistent with a self-sustaining AP train. Trace shows raw waveform (blue), baseline-subtracted moving-average filtered waveform (orange), pulse finding threshold (dashed red), and identified pulse times (green).

4 Towards a cryogenic cosmic ray muon veto system

The main motivation for testing the NUV-HD-cryo SiPM technology in an ultra-low temperature environment is to determine whether it is feasible for SiPMs to be deployed as photon sensors for the cryogenic cosmic ray muon veto system currently being designed for the QUEST-DMC experiment. As outlined in Section 1, the concept design makes use of a scintillator volume surrounding the bolometer box holding the superfluid ^3He target, coupled to a SiPM. High energy cosmic ray muons are minimum ionising particles which deposit approximately 2 MeV/g/cm^2 of energy in materials they traverse. If a cosmic ray muon passes through QUEST-DMC, it will also deposit a fraction of its energy into the scintillator surrounding the experiment, thus producing a flux of scintillation photons. These can be used as a veto signal, to remove any fiducial volume events from the dark matter search that occur in coincidence with a scintillator signal consistent with a cosmic ray muon. If the SiPM is directly coupled to the scintillator (i.e., without using fibres to optically couple the physically separated scintillator and SiPM), it will need to be capable of operating at the same temperature as the scintillator, which is thermally coupled to a thermal radiation shield at a temperature of $O(10\text{s mK})$.

In addition to the main dataset used for the characterisation analysis, we also acquired a second, shorter dataset where a small volume of scintillator was coupled to the SiPM. We acquired 2500

waveforms per voltage under the same trigger conditions as before, with a shorter 10 μ s acquisition window (1 μ s pre-trigger, 9 μ s post-trigger). The plastic scintillator used for this study was an early prototype for the SoLid experiment [24], and is reported to have a scintillation efficiency of approximately 10000 photons/MeV e^- [25]. This was a convenient test sample for the purpose of these initial proof-of-concept measurements.

Three small blocks of the scintillator, each with dimensions 1 cm (W) \times 3 cm (L) \times 0.5 cm (D), are attached to the inside of a spare copper box lid using Araldite. The scintillator blocks are each embedded with three wavelength shifting fibres [26], which shift blue light into green light and guide the photons produced in the scintillator towards the face of the SiPM. Figure 13 shows a picture of the scintillator blocks attached to the inside of the copper box lid. Whilst the SiPM is not physically in contact with the scintillator blocks when the box is closed, there is an extremely small gap of 1-2 mm between the scintillator blocks and the SiPM face when the box is closed. The SiPM sits in the central area of the three scintillator blocks, for maximum coverage and light collection efficiency.

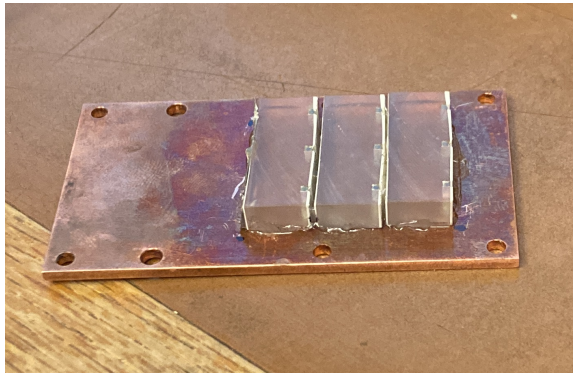


Figure 13. Image showing the three scintillator blocks attached to the inside of the spare copper box lid. Each block is embedded with three optical fibres, which guide photons generated in the scintillator towards the SiPM surface.

Figure 14 (left) shows an example event observed in this dataset, acquired at $V_{bias} = 32$ V ($\Delta V = 4.8$ V). In this event, the number of photons incident on the SiPM is so large that it surpasses the dynamic range of the oscilloscope, illustrated by the clipping of the signal at 140 mV. For high photon fluxes such as this, we also observe a lengthening of the signal tail, compared to the SiPM recharge time (<1 μ s). This is caused by the superposition of pulses from real photons, optical crosstalk, and afterpulsing, which contribute to an overall increase in the duration of the signal.

Figure 14 (right) compares the pulse charge distribution, computed as the 10 μ s integral about the event trigger, for data acquired with the scintillator (red) versus data acquired without the scintillator (blue). Without scintillator, we only expect to observe signals associated with the SiPM's intrinsic noise, resulting in a narrow distribution peaked at the single-photon charge. However, once scintillator is introduced, we observe a much broader distribution and a high charge tail, corresponding to energy depositions in the scintillator from particle interactions. This distribution is likely a combination of environmental gamma-rays, which dominate the lower part of the charge distribution, and high-energy cosmic ray muons populating the high charge tail, as observed in

the cryogenic cosmic ray muon veto system developed by the NUCLEUS experiment [10]. This demonstrates that the SiPM is clearly detecting light from the scintillator and optical fibres, which is easily distinguishable above the SiPM noise sources.

As discussed in Section 3.4.1, the SiPM exhibits an increase in noise from long-lasting APs when operated at ultra-low temperatures. Whilst this additional noise source clearly limits the photon-counting capability of the SiPM for a low photon flux, this is less of a concern for high photon fluxes generated from cosmic ray muons. An increase in long-lasting APs will manifest as an increase to the integrated charge of a signal, but only in response to a primary energy deposition in the scintillator. As such, this should not limit the ability of the SiPM to tag cosmic ray muons through their initial energy deposition. This effect will however need to be fully characterised in order to model the observed charge distribution and determine an appropriate veto threshold. This is a first proof-of-concept of using scintillator directly coupled to a NUV-HD-cryo SiPM in a mK environment as a means of identifying cosmic ray muons.

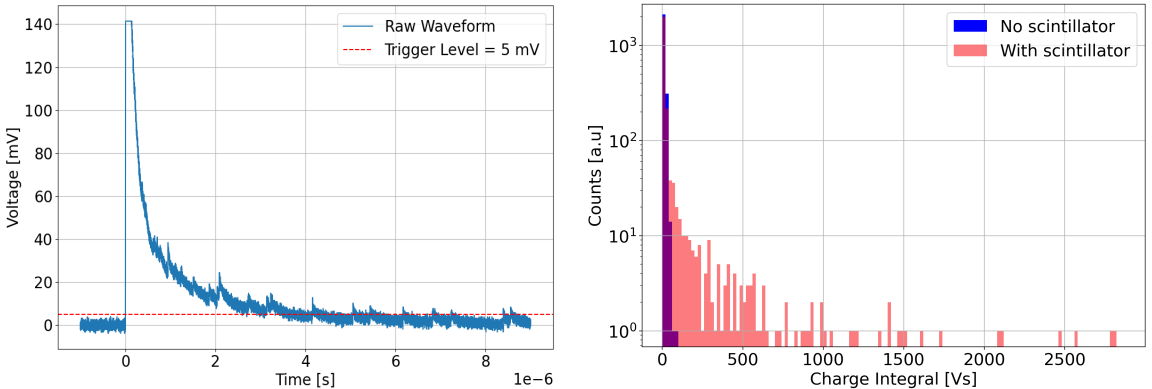


Figure 14. Left: Example waveform trace taken at $V_{\text{bias}} = 32$ V ($\Delta V = 4.8$ V), illustrating a candidate cosmic ray muon event. Right: Pulse charge distribution (integrated over a 10 μs window) about the event trigger at $V_{\text{bias}} = 32$ V ($\Delta V = 4.8$ V) when SiPM is not coupled to scintillator (blue) versus when SiPM is coupled to scintillator (red).

5 Conclusions

We have shown that FBK NUV-HD-cryo SiPMs are capable of operating successfully in a dilution refrigerator, down to a base temperature of 9.4 ± 0.2 mK. We measure the reverse I-V curve of a single SiPM at room temperature and at the base temperature, T_{MC} , determining the breakdown voltage to be $V_{\text{bd,RT}} = 32.18 \pm 0.07$ V and $V_{\text{bd,MC}} = 27.16 \pm 0.05$ V respectively. The observed decrease in the breakdown voltage of the SiPM is consistent with the expected relationship between the breakdown voltage and temperature for this technology. We observe that there is no difference between the measured breakdown voltage at T_{MC} and the average breakdown voltage at 77 K of 27.19 ± 0.05 V measured by the DarkSide-20k collaboration for this technology [16].

We characterise the SiPM operated at T_{MC} as a function of overvoltage, ΔV . We measure the gain of the SiPM to range from 6×10^5 and 9×10^5 for $4.8 \text{ V} < \Delta V < 6.8 \text{ V}$, consistent with typical

SiPM gains of 10^5 – 10^7 . We measure the dark count rate of the SiPM to be 3.89 ± 0.19 mHz/mm² at $\Delta V = 4.8$ V, and observe an increase in the dark count rate of 25% between $\Delta V = 4.8$ V and $\Delta V = 6.8$ V. The dark count rate values we measure are also closely in agreement with the value of <5 mHz/mm² measured at 77 K [11] for this technology, suggesting that for temperatures below 77 K, the dark count rate is dominated by tunnelling effects which are weakly temperature dependent. We measure the mean number of additional prompt avalanches due to direct crosstalk to be $\bar{N}_{\text{APA}} = 0.170 \pm 0.002$ at $\Delta V = 4.8$ V, corresponding to a direct crosstalk probability of $16\% \pm 0.2\%$. We observe an increase in \bar{N}_{APA} of 64% across $4.8 \text{ V} < \Delta V < 6.8$ V. At 77 K, the direct crosstalk probability is reported to be 13% at $\Delta V = 5$ V [11]; whilst this could suggest a small increase in the direct crosstalk probability compared to 77 K, this small difference is more likely an artifact of our data selection and analysis choices.

We measure the average number of correlated delayed avalanches, dominated primarily by afterpulses, for three different integration windows following a primary avalanche. The average number of CDAs is measured to be $\bar{N}_{\text{CDA}} = 0.170 \pm 0.002$ (1 μs window), 0.420 ± 0.003 (5 μs window), and 0.560 ± 0.004 (10 μs window) at $\Delta V = 4.8$ V. \bar{N}_{CDA} increases by 102% (1 μs window), 146% (5 μs window), and 172% (10 μs window) between $\Delta V = 4.8$ V and $\Delta V = 6.8$ V. The afterpulsing probability is reported to be 12% at 77 K [11], compared to our measurement of 43% at $\Delta V = 4.8$ V (assuming a 10 μs integration window). A significant increase in afterpulsing has previously been reported for SiPMs operating at temperatures below 40 K [4, 5], which results in self-sustaining cascades of afterpulses that can last for up to approximately 1 ms at low temperatures. We observe evidence consistent with an increase in long-lasting afterpulses in our data, the effect of which is enhanced for higher ΔV .

Finally, we present initial measurements of deploying a NUV-HD-cryo SiPM coupled to a scintillator with optical fibre assembly, operated down to 9.4 mK, as proof of concept for a cryogenic cosmic ray muon veto system to be operated internal to a dilution refrigerator. In this run, we observe a significantly larger charge spectrum with a high charge tail, consistent with energy depositions from environmental gamma-rays and high-energy cosmic ray muons that are not present in the data acquired without the scintillator. The work presented in this manuscript will be used to inform the final design and optimisation of the cryogenic cosmic ray muon veto system currently under development for the QUEST-DMC experiment.

Acknowledgments

This work was funded by UKRI EPSRC and STFC (Grants ST/T006773/1, ST/Y004434/1, EP/P024203/1, EP/W015730/1 and EP/W028417/1), as well as the European Union’s Horizon 2020 Research and Innovation Programme under Grant Agreement no 824109 (European Microkelvin Platform). S.A. acknowledges financial support from the Jenny and Antti Wihuri Foundation. M.D.T acknowledges financial support from the Royal Academy of Engineering (RF/201819/18/2). J.Sm. acknowledges support from the UK Research and Innovation Future Leader Fellowship MR/Y018656/1. A.K. acknowledges support from the UK Research and Innovation Future Leader Fellowship MR/Y019032/1.

References

- [1] P.-A. Amaudruz et al., *In-situ characterization of the Hamamatsu R5912-HQE photomultiplier tubes used in the DEAP-3600 experiment*, *NIM A* **922** (2019) 373 [[1705.10183](#)].
- [2] D. Akerib et al., *The LUX-ZEPLIN (LZ) experiment*, *NIM A* **953** (2020) 163047 [[1910.09124](#)].
- [3] M. Biroth et al., *Silicon photomultiplier properties at cryogenic temperatures*, *NIM A* **787** (2015) 68.
- [4] O. Hanski et al., *Performance of Silicon photomultipliers at low temperatures*, [2501.03812](#).
- [5] J. Zhang et al., *Scintillation detectors with silicon photomultiplier readout in a dilution refrigerator at temperatures down to 0.2 k*, *JINST* **17** (2022) P06024 [[2203.15631](#)].
- [6] S. Autti et al., *QUEST-DMC superfluid ^3He detector for sub-GeV dark matter*, *EPJC* **84** (2024) 248 [[2310.11304](#)].
- [7] N. Darvishi et al., *Dark matter attenuation effects: sensitivity ceilings for spin-dependent and spin-independent interactions*, *JCAP* **04** (2025) 017 [[2502.10251](#)].
- [8] N. Darvishi et al., *Dark Matter EFT Landscape Probed by QUEST-DMC*, [2505.17995](#).
- [9] S. Autti et al., *QUEST-DMC: background modelling and resulting heat deposit for a superfluid helium-3 bolometer*, *Journal of Low Temperature Physics* **215** (2024) 465 [[2402.00181](#)].
- [10] A. Erhart et al., *A plastic scintillation muon veto for sub-Kelvin temperatures*, *EPJC* **84** (2024) 70 [[2310.08457](#)].
- [11] A. Gola et al., *NUV-sensitive silicon photomultiplier technologies developed at Fondazione Bruno Kessler*, *Sensors* **19** (2019) 308.
- [12] O. Instruments, “Triton Series Brochure.” https://nanoscience.oxinst.com/assets/uploads/products/nanoscience/documents/4640_NS_Triton_Brochure.pdf.
- [13] A. Shibahara et al., *Primary current-sensing noise thermometry in the millikelvin regime*, *Philosophical Transactions of the Royal Society A: Mathematical, Physical and Engineering Sciences* **374** (2016) 20150054.
- [14] J. Nyéki et al., *High-performance cryogen-free platform for microkelvin-range refrigeration*, *Physical Review Applied* **18** (2022) L041002 [[2209.07903](#)].
- [15] Tetroxix, “DPO72304DX Oscilloscope Datasheet.” https://www.rfesolutions.com/pdf/oscilloscopes/DP072304DX--Data_Sheet.pdf.
- [16] F. Acerbi et al., *Quality Assurance and Quality Control of the 26 m² SiPM production for the DarkSide-20k dark matter experiment*, *EPJC* **85** (2025) [[2412.18867](#)].
- [17] Tetroxix, “Using FastFrame™ Segmented Memory.” https://download.tek.com/document/55W_12112_2.pdf.
- [18] Hamamatsu, “What is an SiPM and how does it work?” <https://hub.hamamatsu.com/us/en/technical-notes/mpcc-sipms/what-is-an-SiPM-and-how-does-it-work.html>.
- [19] A. Butcher et al., *A method for characterizing after-pulsing and dark noise of PMTs and SiPMs*, *NIM A* **875** (2017) 87 [[1703.06204](#)].
- [20] R. Mirzoyan et al., *Light emission in Si avalanches*, *NIM A* **610** (2009) 98.
- [21] F. Acerbi et al., *NUV silicon photomultipliers with high detection efficiency and reduced delayed correlated-noise*, *IEEE transactions on Nuclear Science* **62** (2015) 1318.
- [22] F. Acerbi and S. Gundacker, *Understanding and simulating SiPMs*, *NIM A* **926** (2019) 16.

- [23] B. Ridley, *Lucky-drift mechanism for impact ionisation in semiconductors*, *J. Phys. C: Solid State Phys.* **16** (1983) 3373.
- [24] Y. Abreu et al., *Optimisation of the scintillation light collection and uniformity for the SoLid experiment*, *JINST* **13** (2018) P09005 [[1806.02461](https://arxiv.org/abs/1806.02461)].
- [25] E. Technology, “GENERAL PURPOSE EJ-200, EJ-204, EJ-208, EJ-212.” <https://eljentechnology.com/products/plastic-scintillators/ej-200-ej-204-ej-208-ej-212>.
- [26] L. Solutions, “Plastic scintillating fibers.” <https://luxiumsolutions.com/sites/default/files/2021-11/Fiber-Product-Sheet.pdf>.